

Mask-PINNs: Regulating Feature Distributions in Physics-Informed Neural Networks

Feilong Jiang^a Xiaonan Hou^a Jianqiao Ye^a Min Xia^{b*}

^a Department of Engineering, Lancaster University, LA1 4YW Lancaster, U.K.

^b Department of Mechanical and Materials Engineering, University of Western Ontario, London, Ontario, Canada
min.xia@uwo.ca

Abstract

Physics-Informed Neural Networks (PINNs) have emerged as a powerful framework for solving partial differential equations (PDEs) by embedding physical laws directly into the loss function. However, effective training of PINNs remains challenging due to internal covariate shift, which destabilizes feature distributions and impairs model expressiveness—especially in wider architectures. While normalization techniques like Batch Normalization and Layer Normalization are standard remedies in deep learning, they disrupt the pointwise input-output mappings critical to preserving the physical consistency in PINNs. In this work, we introduce Mask-PINNs, a novel architecture that regulates internal feature distributions through a smooth, learnable mask function applied pointwise across hidden layers. Unlike conventional normalization methods, the proposed mask function preserves the deterministic nature of input-output relationships while suppressing activation drift and saturation. Theoretically, we demonstrate that Mask-PINNs control feature spread near initialization by attenuating gradient variance growth through a tailored modulation mechanism. Empirically, we validate the method on multiple PDE benchmarks—including convection, wave propagation, and Helmholtz equations—across diverse activation functions. Our results show consistent improvements in prediction accuracy, convergence stability, and robustness, with relative L^2 errors reduced by up to two orders of magnitude over baseline models. Furthermore, we demonstrate that Mask-PINNs enable the effective use of wider networks, overcoming a key limitation in existing PINN frameworks.

Key words: Deep learning, Physics-informed neural networks, Partial differential equations, Scientific machine learning

1 Introduction

Partial Differential Equations (PDEs) play a central role in modelling dynamic physical phenomena across domains such as physics, engineering, and finance. Recently, Physics-Informed Neural Networks (PINNs) have emerged as a powerful computational framework for solving PDEs by embedding governing equations, along with initial and boundary conditions, directly into the neural network’s loss function [1]. Leveraging automatic differentiation for derivative computation, PINNs can bypass the need for meshing and offer flexibility in handling irregular geometries and high-dimensional problems. Furthermore, their ability to seamlessly integrate observed data makes PINNs particularly valuable in real-world applications where information is often incomplete [2-5]. Due to their strong interpretability and ease of implementation, PINNs have found successful applications in diverse fields such as fluid mechanics [6], heat transfer problem [7], solid mechanics [8], geoen지니어ing [9], chemical engineering [10], finance [11], and climate modelling [12].

Despite their growing popularity, training PINNs effectively remains a substantial challenge. Since their performance strongly depends on activation functions, some researchers proposed algorithms for automatically learning or adapting these functions to enhance training efficiency and stability [13], [14]. Additionally, PINNs are prone to initialization pathologies, which can lead to performance degradation in deeper architectures. To address this, researchers have proposed new architectures such as PirateNets, HyResPINNs, and Deeper-PINNs [15-17]. Another known difficulty is the existence of competing objectives in the composite loss function, often leading to gradient conflicts that hinder convergence; several approaches based on gradient alignment have been proposed to address this issue [18], [19]. Poor initial choices can lead to vanishing or exploding gradients and slow convergence, especially for deeper PINN structures. Consequently, theoretically informed approaches are proposed to ensure stable training and robust convergence in PINNs [20], [21].

One critical issue that remains underexplored is internal covariate shift—the instability of feature distributions during training—which undermines both the learning dynamics and the expressiveness of PINNs [22]. Normalization techniques, such as Batch Normalization (BN) and Layer Normalization (LN), are typically employed to mitigate these issues in conventional deep learning settings. However, these methods rely on batch or feature statistics, which disrupt the input-output mapping and the relative relationships between different inputs. Consequently, there remains a need for effective, physics-compatible methods to regulate feature distributions in PINNs.

In this paper, we propose Mask-PINNs that can fill the gap in alleviating the internal covariate shift of PINNs. We demonstrate that Mask-PINNs can enhance training stability and prediction accuracy across several benchmarks. Our main contributions are summarized as:

- We propose Mask-PINNs, a novel PINN architecture that introduces a learnable, nonlinear mask function to regulate the internal feature distributions of the network. Unlike conventional normalization techniques, the mask function operates in a pointwise and input-conditioned manner, preserving the deterministic input-output relationships essential for enforcing physical constraints.
- We demonstrate that the proposed masking mechanism effectively suppresses feature drift, leading to more centered and stable intermediate representations throughout training. This allows the model to maintain expressiveness without sacrificing physical fidelity.
- Extensive experiments across diverse PDE benchmarks and activation functions show that Mask-PINNs achieve consistent and significant improvements in prediction accuracy and training stability.
- We show that Mask-PINNs enable effective training of wider neural networks, overcoming a critical limitation in conventional PINNs where increasing network width typically leads to performance degradation. This opens new possibilities for scaling PINNs to more complex problems.

The remainder of the paper is organized as follows: Section 2 reviews relevant prior work and discusses key limitations; Section 3 introduces Mask-PINNs in detail; Section 4 presents comprehensive experimental validation; and finally, Section 5 summarizes the findings and discusses potential directions for future research.

2 Background

This section introduces the working principle of PINNs. We also briefly discuss traditional normalization techniques' limitations in PINNs.

2.1 Physics-informed Neural Networks

Given the following partial differential equation (PDE):

$$\mathbf{u}_t + \mathcal{N}[\mathbf{u}(t, x)] = 0, \quad t \in [0, T], \quad x \in \Omega, \quad (1)$$

governed by the initial and boundary conditions:

$$\mathbf{u}(0, x) = \mathbf{u}^0(x), \quad x \in \Omega, \quad (2)$$

$$\mathcal{B}[\mathbf{u}] = 0, \quad t \in [0, T], \quad x \in \partial\Omega, \quad (3)$$

where $\mathbf{u}(t, x)$ indicates the solution, $\mathcal{N}[\cdot]$ represents a linear or nonlinear differential operator, $\mathcal{B}[\cdot]$ indicates boundary operator.

The task of PINNs is approximating the solution of the given PDE by a deep neural network (DNN) $\mathbf{u}_\theta(t, x)$, where θ denotes all trainable parameters. For PINNs, $\mathbf{u}_\theta(t, x)$ is constrained by the following loss function:

$$\mathcal{L}(\theta) = \lambda_{ic} \mathcal{L}_{ic}(\theta) + \lambda_{bc} \mathcal{L}_{bc}(\theta) + \lambda_r \mathcal{L}_r(\theta), \quad (4)$$

where

$$\mathcal{L}_{ic}(\theta) = \frac{1}{N_{ic}} \sum_{i=1}^{N_{ic}} \left| \mathbf{u}_\theta(0, x_{ic}^i) - \mathbf{u}^0(x_{ic}^i) \right|^2, \quad (5)$$

$$\mathcal{L}_{bc}(\theta) = \frac{1}{N_{bc}} \sum_{i=1}^{N_{bc}} \left| \mathcal{B}[\mathbf{u}_\theta](t_{bc}^i, x_{bc}^i) \right|^2, \quad (6)$$

$$\mathcal{L}_r(\theta) = \frac{1}{N_r} \sum_{i=1}^{N_r} \left| \frac{\partial \mathbf{u}_\theta}{\partial t}(t_r^i, x_r^i) + \mathcal{N}[\mathbf{u}_\theta](t_r^i, x_r^i) \right|^2, \quad (7)$$

λ is responsible for balancing the weight of different loss terms.

2.2 Internal Covariate Shift of PINNs

It is well known that during training, the feature distributions at each layer tend to drift — shifting in mean, scale, and shape — a phenomenon referred to as internal covariate shift. For bounded activation functions, the outputs tend to approach their upper or lower limits during training, a phenomenon called saturation issue [23]. It is known to induce gradient vanishing and reduce the nonlinear capacity as the activation functions become practically linear in these saturated regions [24-26]. Although the gradient vanishing issue can be alleviated by unbounded activation functions, some commonly used unbounded activation functions still get impaired by the drifting feature distributions. For example, activation functions like GELU, SiLU, and Softplus, etc. have regions that behave almost linearly as the inputs are located far from the centre. Such regions limit the nonlinear representational capacity of the network [24], [27]. Consequently, the model struggles to capture complex nonlinear patterns. A commonly used method for resolving such an issue is the application of normalization techniques [22], [28], [29]. However, the mean subtraction and variance scaling in the normalization, like BN or LN can destroy the physical relationships between the inputs and outputs of PINNs.

The output of a BN layer can be written as:

$$\hat{h}(\mathbf{x}_i; \mathcal{B}) = \gamma \left(\frac{h(\mathbf{x}_i) - \mu_B}{\sigma_B} \right) + \beta, \quad (8)$$

where $h(\mathbf{x}_i)$ is the pre-activation feature map for input \mathbf{x}_i , \mathcal{B} is the current batch contains \mathbf{x}_i , γ and β are learnable scale and shift.

$$\mu_B = \frac{1}{|\mathcal{B}|} \sum_{\mathbf{x}_j \in \mathcal{B}} h(\mathbf{x}_j), \quad (9)$$

$$\sigma_B^2 = \frac{1}{|\mathcal{B}|} \sum_{\mathbf{x}_j \in \mathcal{B}} (h(\mathbf{x}_j) - \mu_B)^2. \quad (10)$$

Because the batch statistics μ_B and σ_B are computed using all samples in the batch, the normalized output $\hat{h}(\mathbf{x}_i; \mathcal{B})$ is no longer solely a function of \mathbf{x}_i , but also implicitly depends on every $\mathbf{x}_j \in \mathcal{B}$. Consequently, the final output can be expressed as:

$$u(\mathbf{x}_i) = f\left(\mathbf{x}_i; \{\mathbf{x}_j\}_{j \in \mathcal{B}}\right). \quad (11)$$

The output $u(\mathbf{x}_i)$ now depends on the entire batch. Since PINNs rely on computing derivatives of the network output with respect to the input to enforce physical laws, the dependency of $u(\mathbf{x}_i)$ on the entire batch makes it impossible to compute physically accurate derivatives without contamination from other samples. As a result, BN breaks the requirement in PINNs for a deterministic, pointwise mapping from input to output.

LN forces all features to have the same mean and variance, even if they get different inputs, which represent fundamentally different physical meanings. This can reduce or erase the meaningful differences between inputs.

In the following, we empirically demonstrate this issue with experiment on the heat conduction problem:

$$\frac{\partial u}{\partial t} - \frac{\partial^2 u}{\partial x^2} = 0, \quad (x, t) \in [0, 1] \times [0, 1], \quad (12)$$

$$u(x, 0) = \sin(\pi x), \quad x \in [0, 1], \quad (13)$$

$$u(0, t) = u(1, t) = 0, \quad t \in [0, 1], \quad (14)$$

the analytical solution for this problem is:

$$u(x, t) = \sin(\pi x) \cdot \exp(-t\pi^2). \quad (15)$$

All the outcomes are averaged from 5 independent trials. As shown in Fig. 1, BN-based PINN (BN-PINN), and LN-based PINN (LN-PINN) show worse results than Vanilla PINN. For BN-PINN, even though the loss curve decreases during the training, the relative L^2 error curve almost stays flat. This indicates that for PINN with BN, the model is not trained with the given physical constraint. Although LN-PINN obtains consistent decreasing on both and loss relative L^2 error, the accuracy is lower than that of vanilla method. This indicates that LN impairs the model's ability to capture physical details.

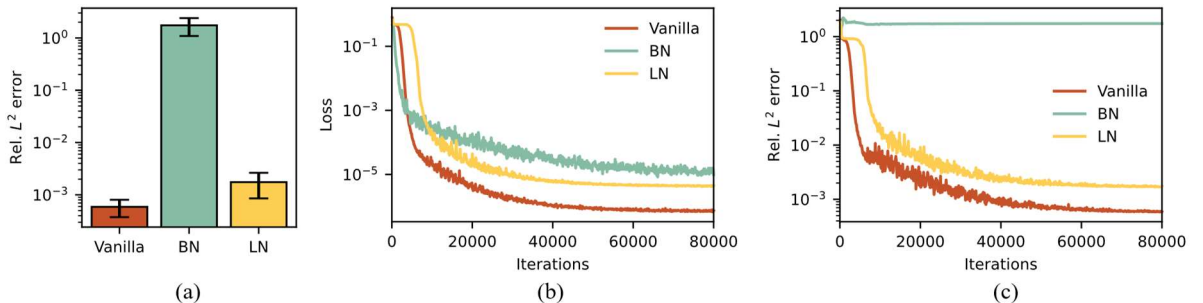


Figure 1. Performance comparison of Vanilla PINN, BN-PINN, and LN-PINN. (a) Mean relative L^2 error. (b) Averaged loss curve. (c) Averaged relative L^2 error curve.

3 Methodology

The motivation behind the proposed method is to reduce internal covariate shift in PINNs while preserving the physical consistency inherent in the input-output relationships. Instead of forcing the feature representations to conform to fixed statistical distributions, as BN and LN do, we propose an input-conditioned modulation mechanism. Fig. 2 shows the schematic illustration of the proposed method. As can be seen, the basic unit of the proposed method is the Mask layer. The key idea of the proposed method is to utilize the specially designed mask function to regulate the output distribution of each hidden layer.

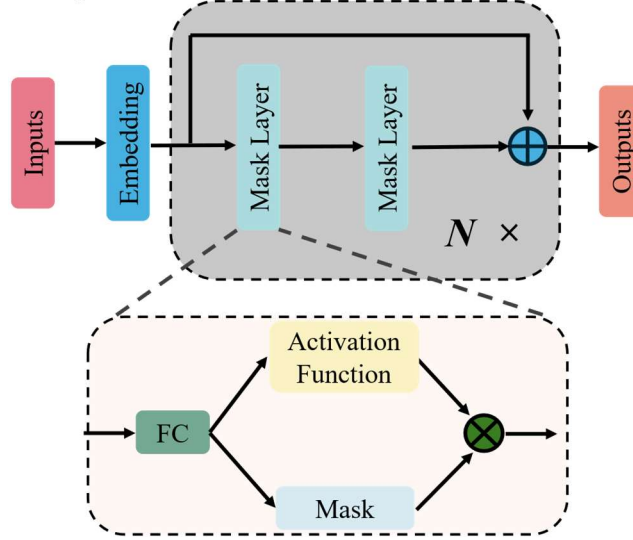


Figure 2. Illustration of the architecture of the Mask-PINNs.

Given an input vector \mathbf{x} , a mask function can be expressed as:

$$F(\mathbf{x}) = 1 - \exp\left[-\boldsymbol{\alpha} \odot \mathbf{x}\right]^2 \quad (16)$$

where $\boldsymbol{\alpha}$ is a learnable vector that controls the sharpness of the mask function. Fig. 3 shows the visualization of the proposed mask function. The proposed mask function, resembling an inverted Gaussian centered at zero, is smooth and differentiable, ensuring the network output remains differentiable as required by PINNs. Besides, the proposed mask function modulates each sample independently, preserving both the deterministic input-output relationship and the relative differences between inputs.

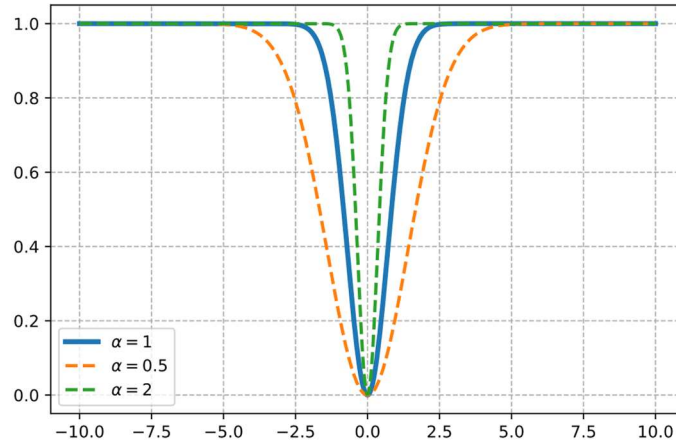


Figure 3. Mask function with different α values. For visualization purposes, we plot the mask function assuming scalar α values, although in practice $\boldsymbol{\alpha}$ is a learnable vector applied independently to each input feature.

To better illustrate how the mask function works, we outline the feed forward process of a block below:

$$z^{(l)} = w^{(l)}H + b^{(l)}, \quad (17)$$

$$H^{(l)} = F^{(l)}(z^{(l)}) \odot \sigma(z^{(l)}), \quad (18)$$

$$\begin{aligned} z^{(l+1)} &= w^{(l+1)}H^{(l)} + b^{(l+1)} \\ &= w^{(l+1)} \left[F^{(l)}(z^{(l)}) \odot \sigma(z^{(l)}) \right] + b^{(l+1)}, \end{aligned} \quad (19)$$

$$H^{(l+1)} = F^{(l+1)}(z^{(l+1)}) \odot \sigma(z^{(l+1)}), \quad (20)$$

where z represents the pre-activation, l is the number of the block, H denotes the output of a layer, w represents weights and b represents biases. As shown in Eq. (19), the distribution of $z^{(2)}$ is influenced by the form and behaviour of $F^{(l)}$, which is designed to control both the scale and spread of the features passed forward.

During the training, the change of the output of a hidden layer can be expressed as:

$$\begin{aligned} \Delta_M &= H(z + \delta) - H(z) \\ &= F(z + \delta) \odot \sigma(z + \delta) - F(z) \odot \sigma(z), \end{aligned} \quad (21)$$

assuming δ is a small change in the pre-activation input z , caused by the update of trainable parameters (i.e., weights and biases).

The first-order Taylor Series Expansion of $H(z + \delta)$ around z can be expressed as:

$$H(z + \delta) = F(z) \odot \sigma(z) + \left[F'(z) \odot \sigma(z) + F(z) \odot \sigma'(z) \right] \delta + O(\delta^2), \quad (22)$$

where the second-order term $O(\delta^2)$ is negligible for small δ . Hence,

$$\Delta_M \approx \left[F'(z) \odot \sigma(z) + F(z) \odot \sigma'(z) \right] \delta, \quad (23)$$

Similarly, for $\sigma(z)$:

$$\Delta \approx \sigma'(z) \delta. \quad (24)$$

By the triangle inequality, the magnitude of Δ_M follows that

$$\|\Delta_M\| \approx \left\| \left[F'(z) \odot \sigma(z) + F(z) \odot \sigma'(z) \right] \delta \right\| \leq \|F'(z) \odot \sigma(z) \delta\| + \|F(z) \odot \sigma'(z) \delta\|. \quad (25)$$

Assuming all weight matrices are initialized by the Glorot, and bias parameters are initialized to zeros. Under such circumstance, the input z is around zero.

The Taylor Series Expansion of $F(z)$ and $F'(z)$ around $z = 0$ are:

$$F(z) = \alpha^2 z^2 + O(z^4) = O(z^2), \quad (26)$$

$$F'(z) = 2\alpha^2 z + O(z^3) = O(z). \quad (27)$$

For commonly used continuous activation functions, the output grows linearly near zero input. Thus, as $z \rightarrow 0$,

$$\sigma(z) = O(z), \quad \sigma'(z) = O(1). \quad (28)$$

Then, we obtain:

$$\|\Delta_M\| \lesssim O(z) \cdot O(z) \delta + O(z^2) \delta = O(z^2) \delta, \quad (29)$$

$$\|\Delta\| \approx O(1) \delta. \quad (30)$$

Therefore, $\|\Delta_M\|$ is approximately 2 orders of magnitude smaller compared to $\|\Delta\|$ around $z = 0$. This result suggests that the proposed mask function effectively suppresses feature spread by controlling the growth rate of the output distribution, as $F(z) \odot \sigma(z)$ grows significantly slower than $\sigma(z)$ around the initialization region. Moreover, the output of the

mask function is designed to be strictly less than 1, which prevents the occurrence of extreme values.

Notice that unlike normalization methods, which are typically applied before the activation function, our mask function is applied alongside it. Such design helps the mask function robustly scale down the feature values. Thinking of placing the mask function before the activation function, we have the output as:

$$H^{(l)} = \sigma(z^{(l)} \odot F^{(l)}(z^{(l)})). \quad (31)$$

Although this may seem to be a more straightforward approach, the distribution of $H^{(l)}$ depends heavily on the properties of the activation function, which can therefore reintroduce the internal covariate shift. For activation functions with $\sigma(0) = 0$ (e.g., Tanh and GELU), this issue is less severe, as their outputs tend to remain approximately Gaussian and zero-centered under Glorot initialization due to their near-linear behaviour around zero.

However, activation functions with $\sigma(0) \neq 0$ (e.g., Sigmoid and Softplus) can introduce a bias shift in the input to the next layer, potentially leading to unstable training and slower convergence [22], [30]. As shown in Eq. (18), when the input is near zero and the mask output is also near zero, the mask function can effectively suppress the output of the activation function and thus reduce the bias shift. Consequently, this choice improves the method’s generalizability across different activation functions.

With the mask function effectively suppressing activation spread and maintaining stable outputs, the network ensures better control over feature distributions. As a result, the input to the subsequent layer, a linear transformation of $H^{(l)}$, exhibits reduced variance and remains more consistently within the nonlinear (non-saturated) operating region of the activation function. This helps maintain effective signal propagation and learning dynamics throughout training.

4 Experiments

To demonstrate the effectiveness of the proposed method, we conducted experiments across several benchmarks. The methods compared against the proposed methods include Vanilla PINNs, ResNet-based PINNs (ResNet-PINN), Weight Normalization-based PINNs (WN-PINNs), locally adaptive activation functions (LAAF) based PINNs, PirateNets, and ABU-PINN. All the methods are trained with Tanh, GELU, SiLU, and SoftPlus as activation functions. Note that ABU-PINN is specifically designed to automatically select activation functions during training, and therefore produces only one result, while the other methods are evaluated separately with each of the four activation functions. Due to the difference in the structure, the depth of each model may vary, but the total trainable parameters are kept about the same. Adam is utilized as the optimizer. All experiments are conducted on a single NVIDIA GeForce RTX 4090 GPU. All results are averaged over 5 independent trials.

4.1 Convection Equation

We consider convection equation expressed as below:

$$\frac{\partial u}{\partial t} + \beta \frac{\partial u}{\partial x} = 0, \quad x \in [0, 2\pi], \quad t \in [0, 1], \quad (32)$$

$$u(0, x) = \sin(x), \quad (33)$$

$$u(t, 0) = u(t, 2\pi), \quad (34)$$

where we set β as 30.

Each model is composed of 13 hidden layers, each containing 256 neurons, and is trained for 50,000 iterations. For the proposed method, α is initialized with all entries set to 1.0.

Table 1 shows the outcomes of different models. The best-performing method under each activation function is underlined, while the overall best result across all methods is highlighted in bold. As can be seen, the proposed method achieves consistent best results among different activation functions. For Tanh, the proposed method achieves performance an error 1 order of magnitude lower than vanilla method. For SoftPlus, the result of the proposed method is 2 orders of magnitude lower than vanilla method.

Table 1: Convection equation: relative L^2 error of different models.

Method	Tanh	GELU	SiLU	SoftPlus
Vanilla	7.29e-3	9.91e-4	1.37e-3	3.55e-1
ResNet-PINN	1.75e-2	1.74e-3	1.50e-3	2.41e-2
LAAF	7.30e-3	9.44e-4	7.23e-4	7.35e-2
PirateNet	1.98e-3	9.73e-3	4.54e-3	1.39e-2
WN-PINNs	3.17e-3	1.02e-3	4.89e-3	5.12e-3
ABU-PINN			2.98e-3	
Mask-PINN	<u>6.93e-4</u>	<u>5.26e-4</u>	<u>4.79e-4</u>	<u>1.66e-3</u>

Fig. 4 compares the pre-activation distributions of the vanilla and proposed methods at the end of training, using SoftPlus as the activation function. As the network goes deeper, the spread of the feature values changes dramatically at the same time, more values shift to the negative side. In contrast, the proposed method shows a much slower change in the scale change and keeps the feature distributions in a Gaussian-like form. This distinct difference between the feature distributions explains why our method yields significantly better performance when using SoftPlus. During training, the vanilla method’s pre-activations tend to drift toward the linear regime of the SoftPlus activation function, which can negatively impact both the training dynamics and the model’s expressiveness.

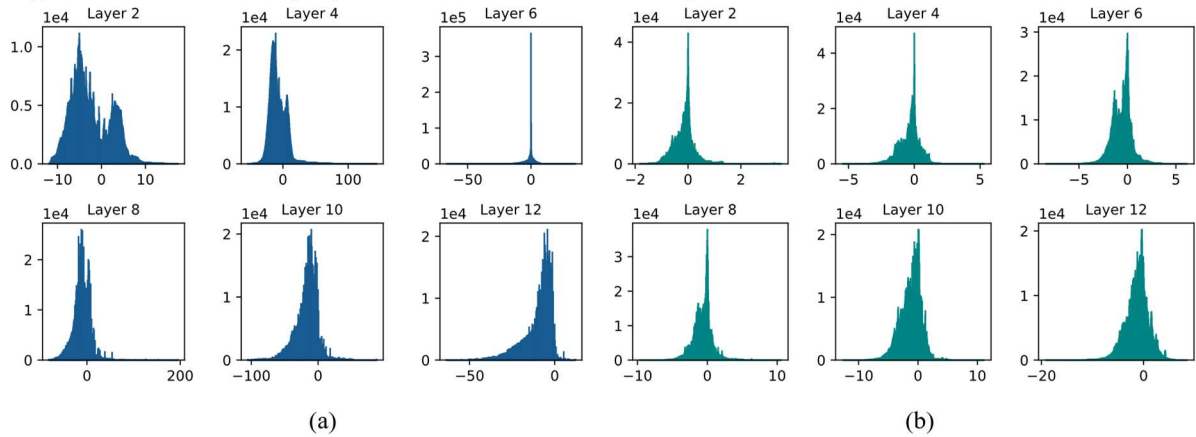


Figure 4. Convection Equation: pre-activation distributions of the vanilla and proposed methods with SoftPlus activation. (a) Vanilla method. (b) Proposed method.

4.2 1D Wave Propagation

Here we consider the 1D wave propagation equation as:

$$\frac{\partial^2 u}{\partial t^2} = c^2 \frac{\partial^2 u}{\partial x^2}, \quad (x, t) \in [0, 1] \times [0, 5], \quad (35)$$

$$u(0, t) = u(1, t) = 0, \quad t \in [0, 5], \quad (36)$$

$$u(x, 0) = \sin(\pi x), \quad x \in [0, 1], \quad (37)$$

$$\frac{\partial u}{\partial t}(x, 0) = 0, \quad (38)$$

the analytical solution for this problem is:

$$u(x, t) = \sin(\pi x) \cos(c\pi t). \quad (39)$$

Here we set $c = 1$. All the models have 7 hidden layers, each containing 256 neurons, and is trained for 20,000 iterations. For the proposed method, α is initialized with all entries set to 1.0.

Table 2 shows the outcomes of different models. Interestingly, while the vanilla method yielded the poorest performance with Tanh, the proposed method achieved its best result using the same activation function. In Fig. 5, we show the variance evolution of the proposed method and vanilla method with Tanh as activation function. The variance for vanilla method increases notably with training, suggesting severe distribution drift. The variance curves of the proposed method show relatively smaller values and stable trends after initial iterations, indicating controlled variance growth. This reflects effective regulation of pre-activations as depth and training progress.

Table 2: 1D Wave propagation: relative L^2 errors of different models.

Method	Tanh	GELU	SiLU	SoftPlus
Vanilla	7.33e-2	5.09e-3	8.52e-3	3.61e-2
ResNet-PINN	4.85e-2	7.52e-3	5.22e-3	7.67e-1
LAAF	1.04e-2	4.37e-3	5.73e-3	1.31e-2
PirateNet	1.59e-2	8.83e-3	9.95e-3	5.04e-2
WN-PINNs	6.14e-2	5.60e-3	7.30e-3	1.46e-1
ABU-PINN		4.82e-2		
Mask-PINN	<u>2.39e-3</u>	<u>2.90e-3</u>	<u>4.82e-3</u>	<u>6.38e-3</u>

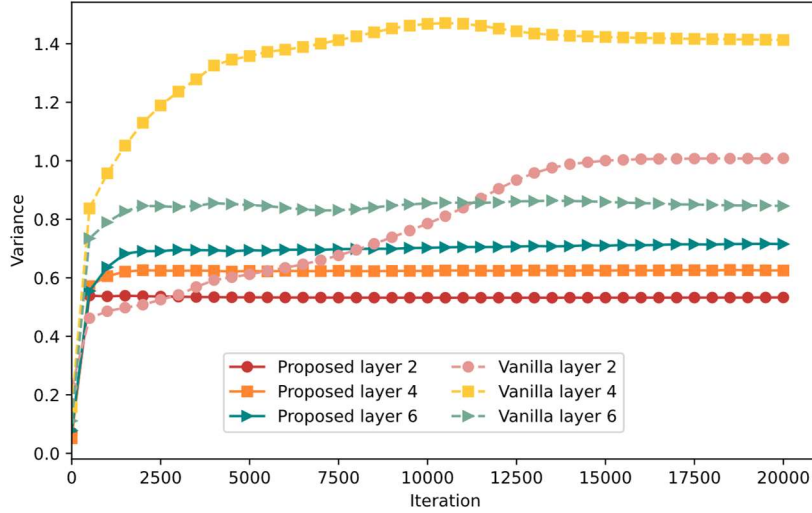


Figure 5. 1D wave propagation equation: variances of pre-activations of vanilla and proposed methods with Tanh activation.

4.3 Helmholtz equation

We consider the Helmholtz equation expressed as below:

$$\frac{\partial^2 u}{\partial x^2} + \frac{\partial^2 u}{\partial y^2} + k^2 u - q(x, y) = 0, \quad x \in [-1, 1], \quad y \in [-1, 1], \quad (40)$$

$$u(-1, y) = u(1, y) = u(x, -1) = u(x, 1) = 0, \quad (41)$$

where the source term $q(x, y)$ is in the form of:

$$\begin{aligned}
 q(x, y) = & -(a_1\pi)\sin(a_1\pi x)\sin(a_2\pi y) \\
 & -(a_2\pi)\sin(a_1\pi x)\sin(a_2\pi y) \\
 & +k^2 \sin(a_1\pi x)\sin(a_2\pi y),
 \end{aligned} \tag{42}$$

here we set $a_1 = 6, a_2 = 6$ and $k = 1$.

All models are composed of 11 hidden layers with 128 neurons each, except PirateNet, which uses 10 hidden layers to keep about the same number of trainable parameters with other methods. Each model is trained for 50,000 iterations. For the proposed method, α is initialized with all entries set to 1.0 for GELU and SiLU, 5.0 for Tanh, and 2.0 for SoftPlus.

Table 3: Helmholtz equation: relative L^2 errors of different models.

Method	Tanh	GELU	SiLU	SoftPlus
Vanilla	9.37e-1	7.20e-1	1.00	1.00
ResNet-PINN	3.48e-1	8.02e-1	7.10e-1	1.00
LAAF	3.26e-2	2.26e-2	1.93e-1	5.89e-1
PirateNet	1.17	3.56e-2	2.68e-1	7.15e-1
WN-PINNs	7.70e-1	7.12e-1	7.12e-1	1.00
ABU-PINN		2.83e-2		
Mask-PINN	<u>9.94e-3</u>	<u>1.52e-2</u>	<u>1.99e-2</u>	<u>1.75e-2</u>

Table 3 shows the outcomes of different models. As can be seen, the proposed method achieves the best performance across different activation functions. Notably, for activation functions SiLU and SoftPlus, other methods fail to get satisfactory results. In contrast, our model maintains comparable accuracy across all activation functions. This highlights its robustness across different activation functions.

As the vanilla method achieves its best performance under GELU, we present the averaged loss curves of different models using GELU as the activation function in Fig. 6. (ABU-PINN is excluded as it dynamically selects activation functions during training.) As shown in Fig. 6, the proposed method converges faster and reaches a lower final loss.

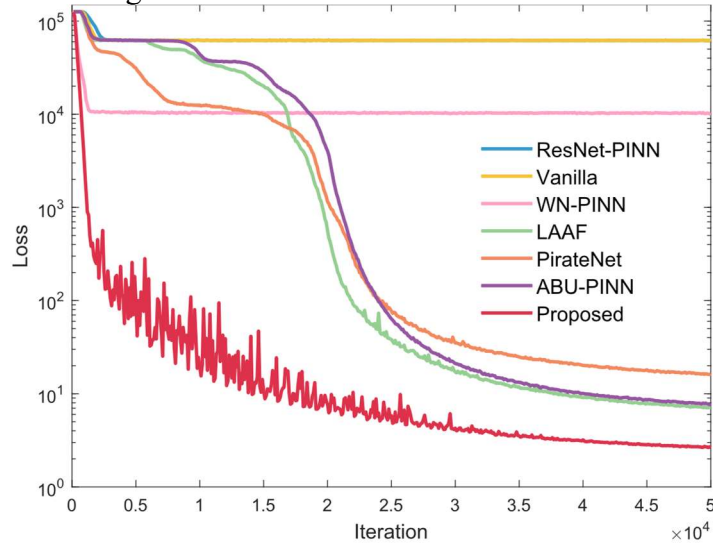


Figure 6. Helmholtz equation: averaged loss curves of different models with GELU as activation function.

Fig. 7 shows the loss landscapes of vanilla method and the proposed method with GELU as activation function. We visualize the loss landscape by perturbing the trained model along the

first two leading eigenvectors of the Hessian and evaluating the loss at each perturbed point. It's evident that the proposed method gets smoother loss landscape. For vanilla method, the surface is highly non-smooth, with many sharp spikes and irregular fluctuations. The irregular and rugged nature of the loss landscape indicates a tendency for the optimizer to become trapped in local minima with high loss value, which is consistent with the loss curve shown in Figure 6.

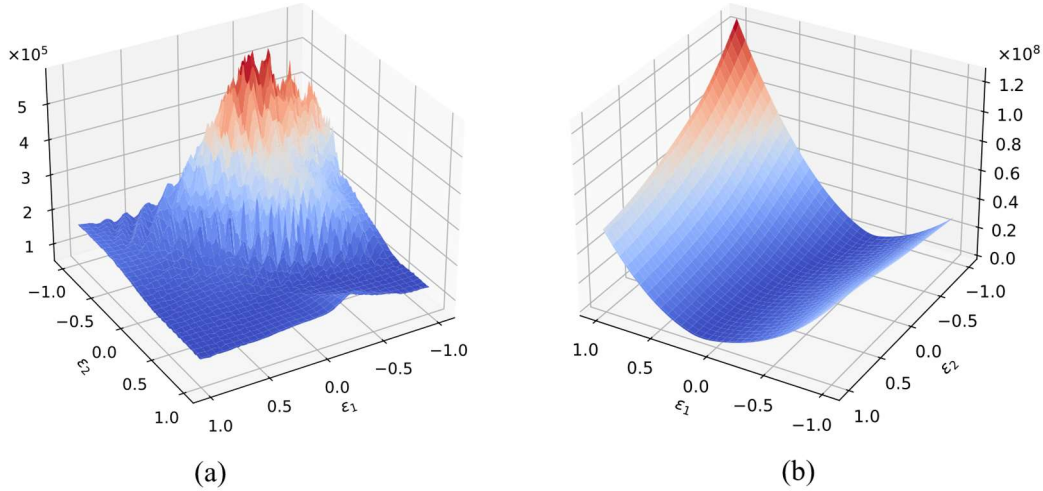


Figure 7. Helmholtz equation: loss landscapes of vanilla method and the proposed method with GELU as activation function. (a) Vanilla method. (b) Proposed method.

4.4 Wider Structure

Although it is commonly known that deeper and wider neural networks can improve approximation capability, for PINNs the situation is quite different. Theoretical analysis and empirical experiments have proven that the PINNs will degrade when the NNs become wider or deeper [15]. While some solutions have been proposed to address the degradation problem in deep PINN architectures [15], [17], [31], the challenge of effectively utilizing wider architectures remains largely unexplored. Here we show that with the proposed method, PINNs can effectively utilize wider structure.

With the Convection equation mentioned above, we conduct experiments on neural networks with different widths across different activation functions. For all the neural networks, we fix the depth to 3 hidden layers. Other settings are aligned with section 4.1. All the results are averaged from 5 independent trials. As shown in Fig. 8, Vanilla PINNs suffer from a degradation issue as the width of the neural network increases. For the proposed method, a consistent improvement is witnessed as the neural network becomes wider. This indicates that the proposed method can mitigate the degradation problem seen in vanilla PINNs. Consequently, it allows PINNs to utilize wider structures, enhancing their robustness and accuracy.

To further explore the underlying reasons behind this improvement, we present the pre-activation distributions of the vanilla and proposed methods in Fig. 9. It clearly shows that with the width increasing, the pre-activation distribution of vanilla PINNs tends to drift away from the center. Also note that for the GELU, SiLU, and SoftPlus activation functions, the pre-activation distributions in the vanilla method exhibit a clear tendency to drift toward the negative range. This suggests that neurons may become inactive or saturated due to these activation functions' asymmetric activation properties, which severely limit the network's expressive power. The proposed method can effectively retain the balanced distribution shape with a narrower variance.

The results presented above highlight that the feature distribution instability and neuron saturation issues of wider neural networks lead to the degradation of PINNs. Our approach directly mitigates these issues by maintaining stable pre-activation distributions, allowing wider architectures to maintain their representational capability and achieve better accuracy.

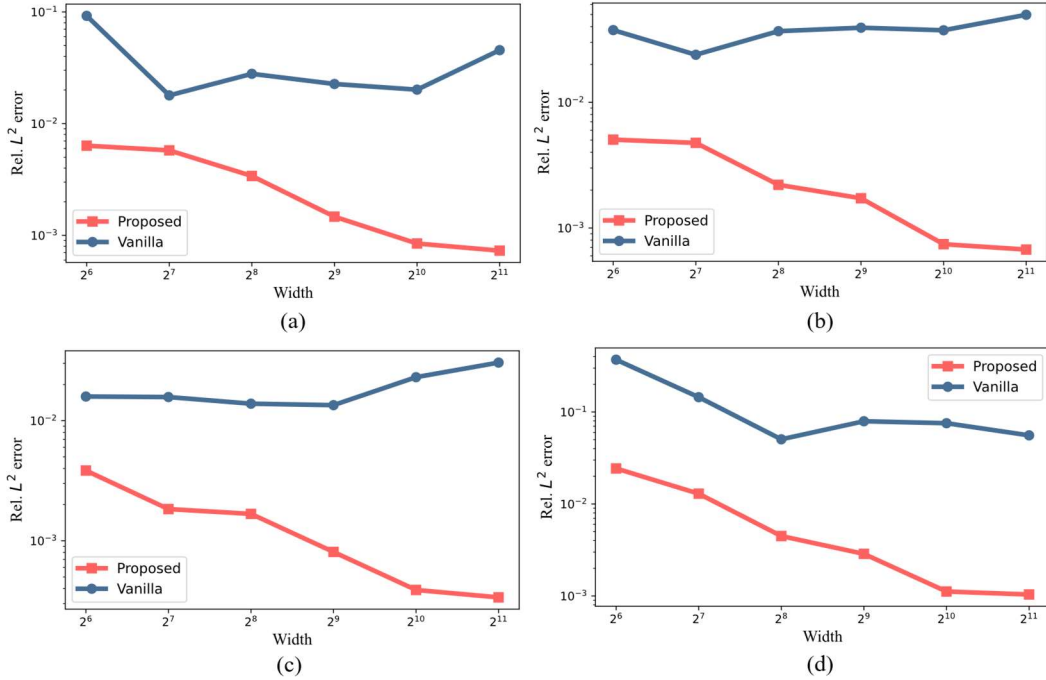


Figure 8. Relative L^2 errors of vanilla PINNs and the proposed method across various network widths. (a) GELU activation function. (b) SiLU activation function. (c) Tanh activation function. (d) SoftPlus activation function.

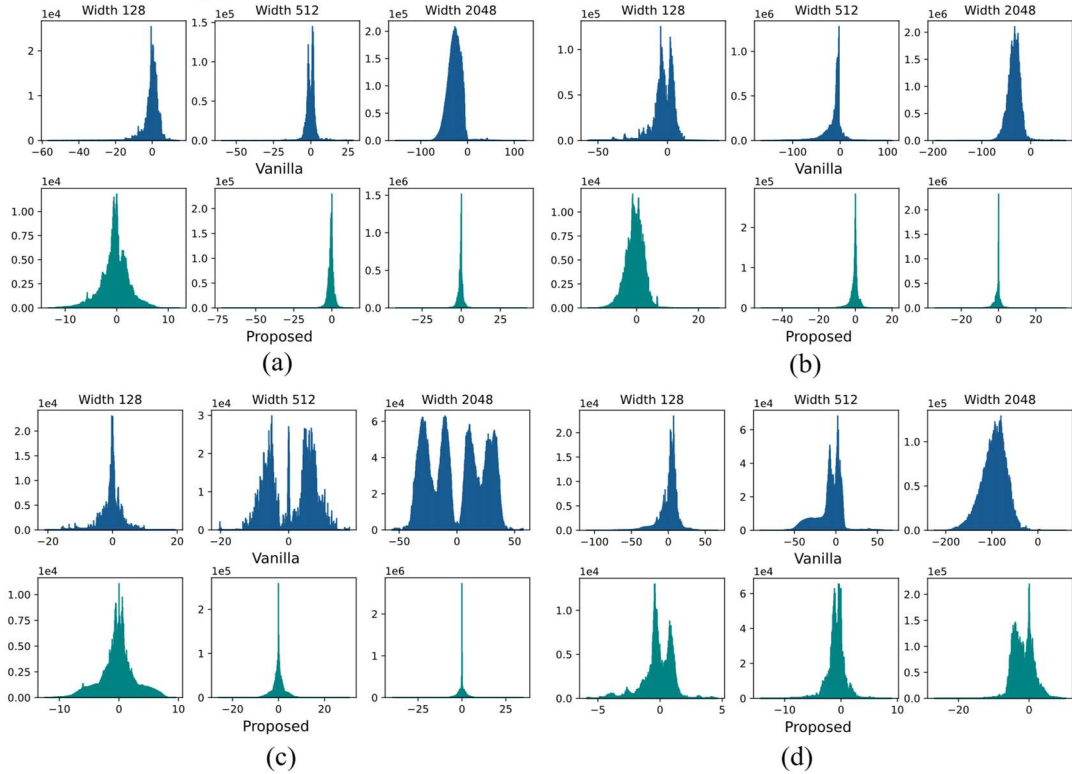


Figure 9. The pre-activation distributions of the 3rd hidden layer at the end of the training. (a) GELU activation function. (b) SiLU activation function. (c) Tanh activation function. (d) SoftPlus activation function.

5 Conclusion

In this paper, we proposed Mask-PINNs, a novel architecture designed to alleviate the issue of internal covariate shift in PINNs without compromising the physical laws embedded in their formulation. By incorporating a smooth, learnable mask function applied pointwise across hidden layers, Mask-PINNs effectively regulate feature distributions, mitigating activation drift. This leads to significantly improved training stability, predictive accuracy, and robustness across a wide range of PDE benchmarks and activation functions. Our experiments demonstrate that Mask-PINNs not only outperform existing methods across different settings but also enable the effective use of wider network architectures. By stabilizing feature distributions, Mask-PINNs provide a simple yet powerful tool for enhancing the representational capability of PINNs. The introduction of Mask-PINNs represents a significant advancement towards stable and scalable neural network architectures for solving PDEs, opening several exciting avenues for future exploration in physics-informed deep learning.

Since the proposed mask function mitigates internal covariate shift while preserving the coordinate-based nature of PINNs, it is worth exploring its applicability to other coordinate-based tasks, such as implicit neural representations [32] and neural radiance fields [33]. While our results are promising, further investigation is needed. Notably, we observed that the initial value of the mask scaling parameter α has a considerable impact on training dynamics. Future research should aim to develop principled initialization strategies for α , tailored to specific tasks and network configurations, to further enhance the reliability and performance of Mask-PINNs.

References

- [1] M. Raissi, P. Perdikaris, and G. E. Karniadakis, "Physics-informed neural networks: A deep learning framework for solving forward and inverse problems involving nonlinear partial differential equations," *Journal of Computational physics*, vol. 378, pp. 686-707, 2019.
- [2] X. Jia *et al.*, "Physics guided RNNs for modeling dynamical systems: A case study in simulating lake temperature profiles," in *Proceedings of the 2019 SIAM international conference on data mining*, 2019: SIAM, pp. 558-566.
- [3] M. Raissi, A. Yazdani, and G. E. Karniadakis, "Hidden fluid mechanics: Learning velocity and pressure fields from flow visualizations," *Science*, vol. 367, no. 6481, pp. 1026-1030, 2020.
- [4] S. Cai *et al.*, "Artificial intelligence velocimetry and microaneurysm-on-a-chip for three-dimensional analysis of blood flow in physiology and disease," *Proceedings of the National Academy of Sciences*, vol. 118, no. 13, p. e2100697118, 2021.
- [5] J. Zhang and X. Zhao, "Three-dimensional spatiotemporal wind field reconstruction based on physics-informed deep learning," *Applied Energy*, vol. 300, p. 117390, 2021.
- [6] S. Cai, Z. Mao, Z. Wang, M. Yin, and G. E. Karniadakis, "Physics-informed neural networks (PINNs) for fluid mechanics: A review," *Acta Mechanica Sinica*, vol. 37, no. 12, pp. 1727-1738, 2021.
- [7] S. Cai, Z. Wang, S. Wang, P. Perdikaris, and G. E. Karniadakis, "Physics-informed neural networks for heat transfer problems," *Journal of Heat Transfer*, vol. 143, no. 6, p. 060801, 2021.
- [8] H. Hu, L. Qi, and X. Chao, "Physics-informed Neural Networks (PINN) for computational solid mechanics: Numerical frameworks and applications," *Thin-Walled Structures*, p. 112495, 2024.

- [9] X.-X. Chen, P. Zhang, and Z.-Y. Yin, "Physics-Informed neural network solver for numerical analysis in geoenvironmental engineering," *Georisk: Assessment and Management of Risk for Engineered Systems and Geohazards*, vol. 18, no. 1, pp. 33-51, 2024.
- [10] Z. Wu, H. Wang, C. He, B. Zhang, T. Xu, and Q. Chen, "The application of physics-informed machine learning in multiphysics modeling in chemical engineering," *Industrial & Engineering Chemistry Research*, vol. 62, no. 44, pp. 18178-18204, 2023.
- [11] Y. Bai, T. Chaolu, and S. Bilige, "The application of improved physics-informed neural network (IPINN) method in finance," *Nonlinear Dynamics*, vol. 107, no. 4, pp. 3655-3667, 2022.
- [12] K. Kashinath *et al.*, "Physics-informed machine learning: case studies for weather and climate modelling," *Philosophical Transactions of the Royal Society A*, vol. 379, no. 2194, p. 20200093, 2021.
- [13] H. Wang, L. Lu, and G. Huang, "Learning Specialized Activation Functions for Physics-Informed Neural Networks," *Communications in Computational Physics*, vol. 34, no. 4, pp. 869-906, 2023.
- [14] J. Zhang and C. Ding, "Simple yet effective adaptive activation functions for physics-informed neural networks," *Computer Physics Communications*, vol. 307, p. 109428, 2025.
- [15] S. Wang, B. Li, Y. Chen, and P. Perdikaris, "PirateNets: Physics-informed Deep Learning with Residual Adaptive Networks," *arXiv preprint arXiv:2402.00326*, 2024.
- [16] M. Cooley, R. M. Kirby, S. Zhe, and V. Shankar, "HyResPINNs: Adaptive Hybrid Residual Networks for Learning Optimal Combinations of Neural and RBF Components for Physics-Informed Modeling," *arXiv preprint arXiv:2410.03573*, 2024.
- [17] F. Jiang, X. Hou, and M. Xia, "Element-wise multiplication based deeper physics-informed neural networks," *arXiv preprint arXiv:2406.04170*, 2024.
- [18] S. Wang, A. K. Bhartari, B. Li, and P. Perdikaris, "Gradient Alignment in Physics-informed Neural Networks: A Second-Order Optimization Perspective," *arXiv preprint arXiv:2502.00604*, 2025.
- [19] Q. Liu, M. Chu, and N. Thuerey, "Config: Towards conflict-free training of physics informed neural networks," *arXiv preprint arXiv:2408.11104*, 2024.
- [20] V. Sitzmann, J. Martel, A. Bergman, D. Lindell, and G. Wetzstein, "Implicit neural representations with periodic activation functions," *Advances in neural information processing systems*, vol. 33, pp. 7462-7473, 2020.
- [21] H. woo Lee, H. Choi, and H. Kim, "Robust Weight Initialization for Tanh Neural Networks with Fixed Point Analysis," in *The Thirteenth International Conference on Learning Representations*.
- [22] S. Ioffe and C. Szegedy, "Batch normalization: accelerating deep network training by reducing internal covariate shift," presented at the Proceedings of the 32nd International Conference on International Conference on Machine Learning - Volume 37, Lille, France, 2015.
- [23] C. Nwankpa, W. Ijomah, A. Gachagan, and S. Marshall, "Activation functions: Comparison of trends in practice and research for deep learning," *arXiv preprint arXiv:1811.03378*, 2018.
- [24] S. R. Dubey, S. K. Singh, and B. B. Chaudhuri, "Activation functions in deep learning: A comprehensive survey and benchmark," *Neurocomputing*, vol. 503, pp. 92-108, 2022.
- [25] C. Tsvetkov, G. Malhotra, B. D. Evans, and J. S. Bowers, "The role of capacity constraints in Convolutional Neural Networks for learning random versus natural data," *Neural Networks*, vol. 161, pp. 515-524, 2023.

- [26] X. Glorot and Y. Bengio, "Understanding the difficulty of training deep feedforward neural networks," in *Proceedings of the thirteenth international conference on artificial intelligence and statistics*, 2010: JMLR Workshop and Conference Proceedings, pp. 249-256.
- [27] M. Lee, "Mathematical analysis and performance evaluation of the gelu activation function in deep learning," *Journal of Mathematics*, vol. 2023, no. 1, p. 4229924, 2023.
- [28] J. L. Ba, "Layer normalization," *arXiv preprint arXiv:1607.06450*, 2016.
- [29] T. Salimans and D. P. Kingma, "Weight normalization: A simple reparameterization to accelerate training of deep neural networks," *Advances in neural information processing systems*, vol. 29, 2016.
- [30] L. Xiangyang, Q. Xing, Z. Han, and C. Feng, "A novel activation function of deep neural network," *Scientific Programming*, vol. 2023, no. 1, p. 3873561, 2023.
- [31] A. Aygun, R. Maulik, and A. Karakus, "Physics-informed neural networks for mesh deformation with exact boundary enforcement," *Engineering Applications of Artificial Intelligence*, vol. 125, p. 106660, 2023.
- [32] J. J. Park, P. Florence, J. Straub, R. Newcombe, and S. Lovegrove, "Deepsdf: Learning continuous signed distance functions for shape representation," in *Proceedings of the IEEE/CVF conference on computer vision and pattern recognition*, 2019, pp. 165-174.
- [33] B. Mildenhall, P. P. Srinivasan, M. Tancik, J. T. Barron, R. Ramamoorthi, and R. Ng, "Nerf: Representing scenes as neural radiance fields for view synthesis," *Communications of the ACM*, vol. 65, no. 1, pp. 99-106, 2021.